Letter

Coexistence of polar and antipolar phases in ferroelectric halide perovskite $CsGeBr_3$

Ravi Kashikar,* S. Lisenkov, and I. Ponomareva†
Department of Physics, University of South Florida, Tampa, Florida 33620, USA

(Received 6 June 2023; revised 7 September 2023; accepted 14 December 2023; published 16 January 2024)

Recently, ferroelectricity has been demonstrated in the family of halide perovskites $CsGeX_3$ (X = Cl, Br, I). We develop a first-principles-based computational approach to probe the finite-temperature properties of $CsGeBr_3$. Our computations reveal the existence of a dynamic antipolar phase above the Curie temperature. The phase can be stabilized below the Curie temperature through quenching. Furthermore, competition between the polar and antipolar phases results in the formation of rare polar-antipolar domains. We demonstrate that such polar-antipolar domains can result in the formation of unusual polarization fields with head-to-head and tail-to-tail dipole arrangements, which not only offers an explanation for the recent experimental findings but could also lead to the discovery of unusual topological polar structures.

DOI: 10.1103/PhysRevB.109.L020101

Inorganic halide perovskites of the form ABX_3, where A = Cs or Rb, B = Ge, Sn, Pb, and X = Cl, Br, I, have gained significant attention because of their optoelectronic properties [1–3]. These perovskites exhibit direct band gaps, low thermal conductivity, high absorption coefficients, high carrier mobility, and long carrier diffusion lengths [4]. These properties find applications in solar cells, light-emitting diodes, semiconductor lasers, photocatalysts, and memristors. These properties are further tunable with composition alterations and external fields, such as pressure, uniaxial strain, and biaxial strain [5–7]. The general structural arrangement consists of BX_6 octahedral cages surrounded by an A site entity. Many halide perovskites undergo phase transitions under pressure and/or temperature to lower-symmetry phases [8,9]. Among these, Sn- and Pb-based crystal phases are centrosymmetric in nature and have multiple phase transitions with temperature [9]. For example, $CsSnX_3$ and $CsPbX_3$ exhibit cubic to tetragonal and tetragonal to orthorhombic phase transitions due to octahedral rotations because their Goldschmidt tolerance factor is less than 1. For $CsGeBr_3$ and $CsGeCl_3$, the tolerance factor is greater than 1, which favors the B site displacements and leads to stabilization of the polar phase. Ge-based perovskites have been proposed to exhibit order-disorder single-phase transitions from a cubic $Pm\bar{3}m$ phase to a polar $R3m$ phase at 428, 511, and 550 K for X = Cl, Br, and I, respectively [10]. Recent experiments have demonstrated ferroelectricity in $CsGeX_3$ (X = Cl, Br, I) and a reported spontaneous polarization of 12–15 $\mu C/cm^2$ for X = Br, and 20 $\mu C/cm^2$ for X = I [11]. So far, there are no experimental polarization reports for X = Cl. With this, $CsGeX_3$ are the only inorganic halide perovskites where the ferroelectricity has been demonstrated experimentally. Furthermore, the band gap of these materials lies between 1.6 and 3.3 eV and is suitable for ferroelectric semiconducting devices [11].

At the moment, an understanding of the ferroelectric phase transitions in these materials is limited. How do the order parameters emerge and evolve with temperature? What is the character of the phase transition and its order? How does the material's response to the electric field depend on the temperature? Does the phase transition in this family have some distinct features? Are there any hidden phases or unusual domains/structures? Do the phase transitions have unique dynamical signatures? Atomistic first-principles-based simulations, such as the effective Hamiltonian [12,13], are an excellent tool to probe the atomistic nature of the phase transitions in complex ferroics and answer some of the aforementioned fundamental questions. Such methodology has previously been used to study phase transitions in ferroelectrics [12,14], ferroelectric alloys [15–18], multiferroics [19], antiferroelectrics [20], and predict novel phases and phenomena such as ferroelectric vortices [21,22], nanostripes [23], bubbles [24,25], ferroelectric phases in antiferroelectrics [26], and electromagnons [27] to name a few.

In this Letter, we aim for the following: (i) to develop an effective Hamiltonian approach to study the finite-temperature properties of $CsGeBr_3$; (ii) to utilize this approach to probe ferroelectricity and the associated phase transition in this material in order to answer some of the fundamental questions raised above; (iii) to predict the existence of both polar and antipolar phases in $CsGeBr_3$; and (iv) to reveal the possibility of these phase coexistence leading to the formation of polar-antipolar domains, which result in unusual polarization fields.

We begin by investigating the phonon instabilities in the cubic phase of $CsGeBr_3$ using density functional theory (DFT) computations as implemented in the VASP package [28,29]. Technically, we use the projector augmented-wave (PAW) basis set [30] within the generalized gradient approximation of Perdew-Burke-Ernzerhof (GGA-PBE) [31]. A plane-wave energy cutoff of 550 eV and a k-point grid density of 0.2 $Å^{-1}$ were used for all our ground state calculations. However, for computing phonon dispersions, elastic constants and a macroscopic dielectric tensor higher-energy cutoff (800 eV) and denser k-point mesh ($16 \times 16 \times 16$)

*ravik@usf.edu
†iponomar@usf.edu

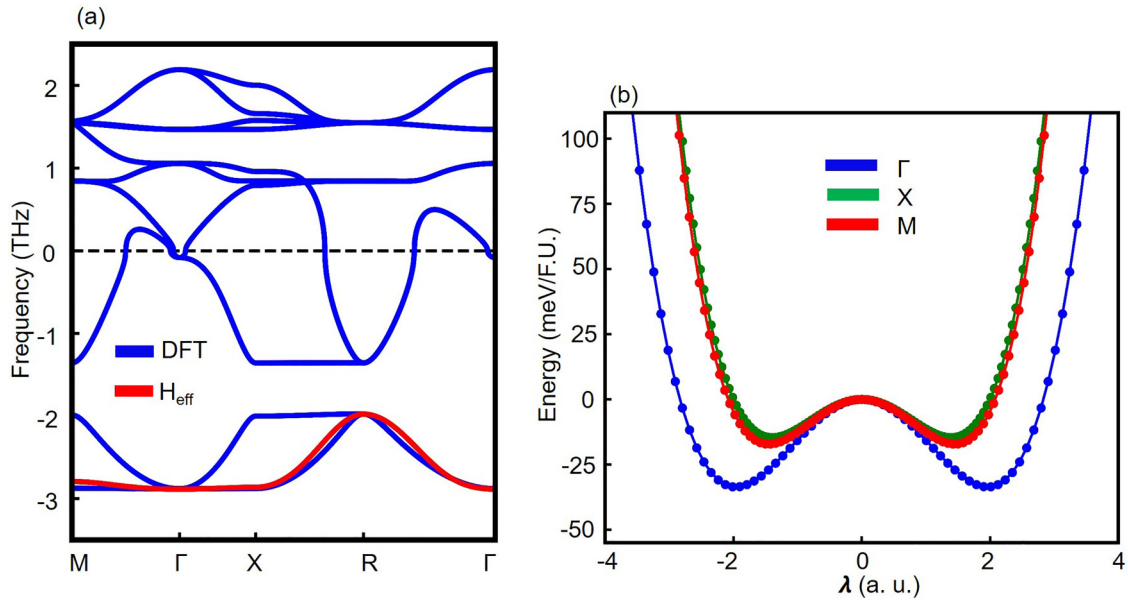

FIG. 1. (a) Phonon dispersion of $CsGeBr_3$ computed from DFT and the effective Hamiltonian (H_{eff}). (b) Energy along the directions of the $CsGeBr_3$ unstable modes at Γ, M, and X.

were used to ensure convergence of the above-mentioned properties. Figure 1(a) reports the phonon dispersion for the cubic $Pm\bar{3}m$ phase of $CsGeBr_3$ computed using density functional perturbation theory (DFPT) and postprocessed using the PHONOPY package [32]. The phonon dispersion predicts the existence of an unstable branch with the strongest instabilities in the Γ, X, and M points. This is in agreement with previous computational findings [9].

Note that we have also used the local density approximation (LDA) exchange-correlation functional [33]. However, we found that it predicts the cubic phase to be more stable than $R3m$ (which contradicts the experiment), and the computed phonon dispersion within the LDA approximation does not possess unstable modes. Therefore, we use the PBE approach for our methodological developments. Next, we compute the energy profile along the eigenvector direction of the unstable phonons at the Γ, X, and M points. The associated energy landscape is given in Fig. 1(b) and suggests the existence of metastable phases in this material, that is, the phases of local minima at the energy surface. The structures that correspond to the minima for the Γ, X, and M point instabilities in Fig. 1 are subjected to a full structural relaxation, which resulted in the following phases: $R3m$ (R), $Pmma$ (O), and $P4/nmm$ (T) with energies with respect to the cubic one of −86.1, −29.7, and −25.9 meV/f.u., respectively. These structures are associated with the antipolar arrangements of Ge and Br ions and are provided in Ref. [34].

Next, we use DFT calculations to parametrize the effective Hamiltonian model of Ref. [13]. The degrees of freedom for the effective Hamiltonian are local modes $\mathbf{u}_i$ (which are proportional to the local dipole moment of the unit cell i), and homogeneous and inhomogeneous strains η_l. The Hamiltonian is written as [13].

$$E_{\text{tot}} = E_{\text{self}}(\{\mathbf{u}_i\}) + E_{\text{dpl}}(\{\mathbf{u}_i\}) + E_{\text{short}}(\{\mathbf{u}_i\}) + E_{\text{elas}}(\{\eta_i\}) + E_{\text{int}}(\{\mathbf{u}_i\}, \{\eta_i\}).$$

The terms on the right-hand side are the local mode self-energy (harmonic and anharmonic contributions), long-range dipole-dipole interactions, a short-range interaction between local modes, elastic energy, and the interaction between the local modes and strains. More details of the effective Hamiltonian terms are given in the Supplemental Material [35] and Ref. [13]. We use the eigenvector of the unstable mode at the Γ point to parametrize our Hamiltonian. The vector is dominated by Ge displacement (see Table I), so we center the local modes on Ge. To parametrize the mass of the local mode, we use the approach of Ref. [36]. An effective Hamiltonian can be utilized in the framework of Monte Carlo, molecular dynamics (MD), and other techniques to simulate finite-temperature properties and has a long history of success [13,14,16,18,19,37].

The parameters of the effective Hamiltonian that we derived for $CsGeBr_3$ are given in Table I and can be used with the publicly available software FERAM [38,39]. We note that the set of parameters reproduces well the lowest-energy phonon branch shown in Fig. 1(a). Table II compares predictions of the effective Hamiltonian with DFT and some available experimental data and demonstrates its accuracy, including in capturing the dynamics of the soft mode.

We now use the effective Hamiltonian in the framework of classical MD simulations to model the finite-temperature properties of bulk $CsGeBr_3$. We use a supercell of $30 \times 30 \times 30$ unit cells of $CsGeBr_3$ repeated periodically along three Cartesian directions. The integration step is 0.5 fs. The Evans-Hoover [40] thermostat is used to simulate constant temperature. A simulated annealing technique is chosen to obtain equilibrium phases at different temperatures. Technically, we start simulations at 600 K and proceed in steps of 10 K down to 10 K. For each temperature, we performed 500 000 MD steps (0.25 ns) and used half of them for equilibration and half for computing thermal averages. The polarization is

TABLE I. First-principles-based parameters for $CsGeBr_3$ in atomic units using the notations of Ref. [13] obtained using the PBE functional.

On-site	κ_2	3.29×10^{-3}	α	5.61×10^{-2}	γ	-9.01×10^{-2}
	j_1	-2.56×10^{-3}	j_2	7.34×10^{-4}		
Intersite	j_3	8.96×10^{-4}	j_4	-4.62×10^{-4}	j_5	4.67×10^{-4}
	j_6	2.12×10^{-4}	j_7	0.00		
Elastic	B_{11}	1.91	B_{12}	0.42	B_{44}	0.39
Coupling	B_{1xx}	−0.48	B_{1yy}	−0.16	B_{5xz}	−0.07
Other	Z^*	7.69	ϵ_∞	7.11	m	46.96
	a (Å)	5.61				
Eigenvector of the unstable mode			(−0.01, −0.75, 0.66, 0.05, 0.05)			

computed as the average dipole moment of the supercell per its volume. Its temperature evolution is given in Fig. 2(a) and predicts a phase transition from the nonpolar $Pm\bar{3}m$ cubic phase to ferroelectric $R3m$ phase at 270 K. The only experimental report to date reports the transition between $Pm\bar{3}m$ and $R3m$ phase at 511 K on the basis of x-ray diffraction and Raman spectroscopy [10,11]. It appears that our effective Hamiltonian underestimates the transition temperature, which is rather common [13,41,42]. At least part of it could be due to the underestimation of the energy difference between the ground state and cubic phase as compared with the DFT data (see Table II). In fact, the difference of 150 K between the effective Hamiltonian and DFT values could account for the underestimation. Another contribution could be due to the dependence of the energy prediction on the exchange-correlation functional [42–45]. Indeed, parametrization with the regularized-restored strongly constrained and appropriately normed (r^2SCAN) functional [46] resulted in an increase of T_C by 70 K. The effective Hamiltonian parameters obtained from the r^2SCAN functional are reported in the Supplemental Material [35]. We notice that the steep onset of the order parameter (polarization) at the Curie point is suggestive of the first-order character of the phase transition.

To elucidate the response of polarization to the electric field, we have computed electric hysteresis loops by applying an ac electric field with frequencies of 1.0, 2.5, 5.0, and 10.0 GHz for all temperatures investigated and show some representative ones in Fig. 2(c). For an ac field frequency of 1 GHz, we find ferroelectric loops up to 295 K, a paraelectric response in the range of 300–400 K, and a linear dielectric response for higher temperatures. The loops are used to compute the remnant polarization as a function of temperature and added to Fig. 2(a). From the comparison between spontaneous and remnant polarization in Fig. 2(a), we notice that ferroelectricity can be stabilized by the electric field in the temperature range of 270–300 K. The coercive field as a function of temperature is reported in Fig. 2(d). We note that the coercive field in computations typically overestimates the experimental one due to the lack of defects in simulated supercells, their finite size, and high frequency of the applied fields. Nevertheless, the comparison between the experimental and our computational coercive field is good [see Fig. 2(d)], which further validates our computational approach. The inset to Fig. 2(d) shows the comparison between computational and experimental hysteresis loops.

The temperature evolution of the lattice parameters is given in Fig. 2(b) and predicts a somewhat unusual dependence. First, it does not follow the first-order-like trend exhibited by polarization. The second feature is the dependence on temperature in the $Pm\bar{3}m$ phase. In our model, the temperature evolution of the lattice parameters originates from the temperature evolution of the local modes owing to the on-site coupling between the local modes and local strains. Therefore, the computational data suggest that the local modes are nonzero even above T_C and even cooperate with each other in some way, which, however, does not result in macroscopic polarization. To elucidate the origin of this unusual behavior, we compute the probability density functions $\rho(u_i)$ for the Cartesian components of the local modes. Technically, we ran an additional 50 000 MD steps on the equilibrated supercells in the temperature range of 250–600 K and used them to obtain probability density functions. Some representative functions are shown in Fig. 3(a) and reveal the presence of two maxima in the functions. Next, we compute the probability density functions for the average local modes, $\rho(\langle u_i \rangle)$, where the average is taken over 50 000 MD steps. The representative functions are shown in Fig. 3(b) and reveal that the two peaks have now merged into a single one, which suggests their dynamic nature. We note that this finding also means that experimentally, the phase would indeed appear as $Pm\bar{3}m$. To probe further into the origin of the peaks in $\rho(u_i)$, we quench the equilibrium supercells that correspond

TABLE II. Some properties of $CsGeBr_3$ as obtained from DFT, the effective Hamiltonian (H_{eff}), and experiment (Expt.). The experimental data are reported for room temperature (RT) and taken from Ref. [11]. The energies are reported with respect to the cubic phase, while * indicates the estimate for the energy difference between the two phases from the Curie point.

	ΔE_T (K)	ΔE_O (K)	ΔE_R (K)	a (Å)	P_S (μC/cm^2)	ω_E (cm^{-1})	ω_{A_1} (cm^{-1})
DFT	−301	−345	−999	5.75	19.9	130.4	160.8
H_{eff}	−242	−285	−862	5.72	23.4	141.5	160.8
Expt.			−511*	5.63	12–15 (RT)	138	163

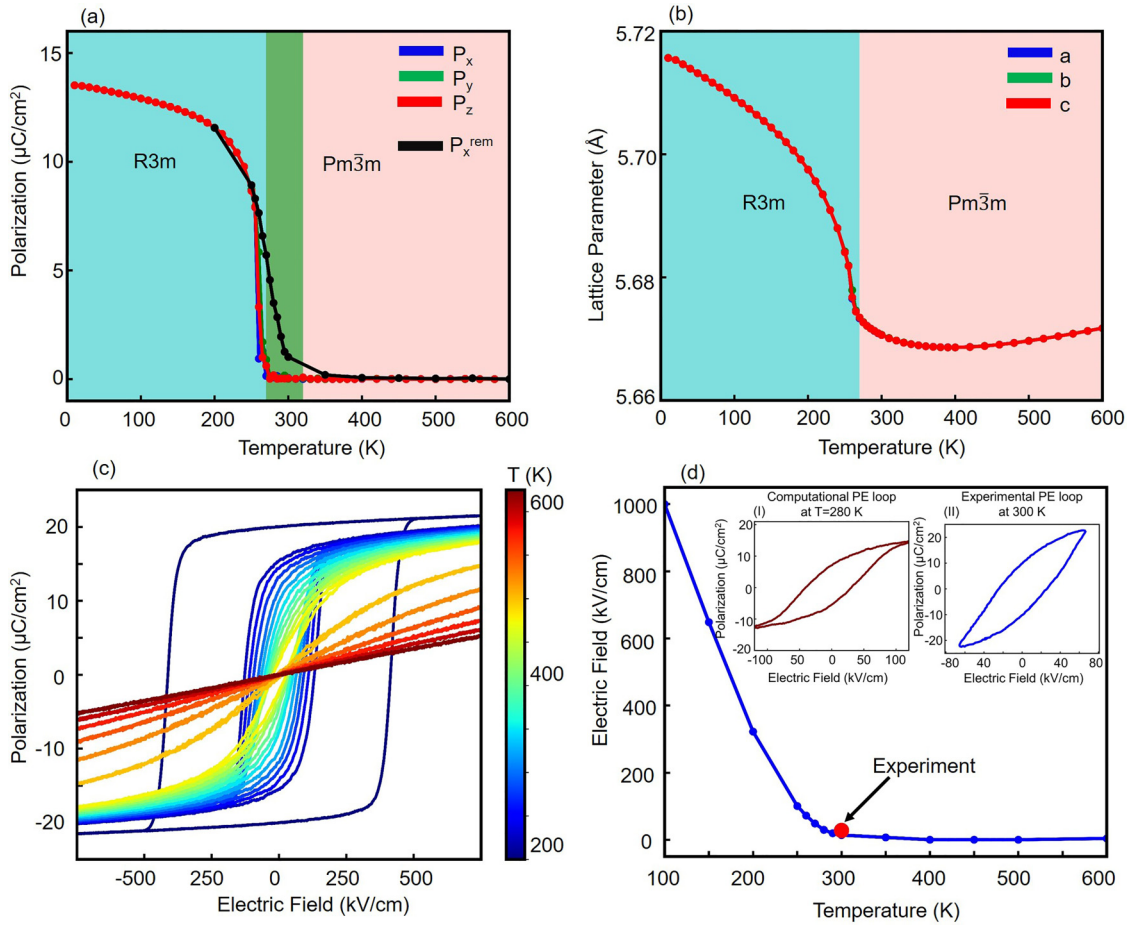

FIG. 2. (a) Polarization components and (b) lattice parameters as a function of temperature. In (a), $P_{x,y,z}$ are the Cartesian components of spontaneous polarization computed from simulated annealing. Black data give one Cartesian component of remnant polarization obtained from hysteresis loops. Green shading outlines the region where the polar phase is stabilized by the electric field. (c) Hysteresis loops computed at 1 GHz frequency in the 200–600 K temperature range. (d) Coercive field as a function of temperature. The inset compares the hysteresis loops at $T = 280$ K with the RT experimental loop reported in Ref. [11].

to temperatures from the 350–600 K range down to 100 K. The probability density functions at 100 K are given in Fig. 3(c) and exhibit two well-defined peaks, whose presence proves that quenching stabilizes the dynamical phase that exists above T_C. Inspection of the quenched dipole patterns reveals antipolar domains, which suggests that the dynamic high-temperature phase is the antipolar one. Recall that the antipolar *Pmma* (O) and $P4/nmm$ (T) phases are also predicted in DFT computations. Furthermore, the stabilization of antipolar domains as opposed to the single-domain phase may suggest that the high-temperature dynamical phase is made up of antipolar nanoregions, a concept similar to the famous polar nanoregions in relaxors [47,48]. Interestingly, such dynamical antipolar domains, or antipolar nanoregions, could explain why the transition in $CsGeBr_3$ is believed to be of order-disorder type [10].

So far, we learned from simulations that annealing results in the stabilization of the polar ground state, while ultrafast quenching yields the antipolar phase with domains. Could the two phases coexist? To answer this question, we carried out quenching with a lower cooling rate; that is, we quenched the supercell from 600 K down to 100 K in steps of 50 K, using 50 000 MD steps for each temperature. Indeed, in this case, we find the coexistence of polar and antipolar domains as shown in Fig. 3(d), which, to the best of our knowledge, is extremely rare. The possibility of the coexistence of polar and antipolar domains has been considered in hafnia films [49]. Moreover, such a coexistence leads to the formation of head-to-head and tail-to-tail domains, as shown in Fig. 3(d), which are energetically unfavored in traditional ferroelectrics. Interestingly, head-to-head domains have indeed been observed experimentally in $CsGeBr_3$ [11]. Moreover, the stabilization of such unusual domains could also mean that new topological polar phases could be discovered in the materials with polar/antipolar phase competition. Experimentally, the stabilization of polar-antipolar domains may be induced by the thermal history. For example, the samples that have not been annealed or not annealed to high enough temperatures may exhibit polar-antipolar domains similar to the ones predicted in simulations. We note that for the simulation cell considered here, as well as for the smaller one of $20 \times 20 \times 20$, we find domain walls, which appear straight in the 2D cross sections. For a larger supercell of $50 \times 50 \times 50$, we encountered domains with somewhat irregular boundaries [35]. We note that all the main findings have been reproduced with parameters obtained with the r^{2}SCAN functional.

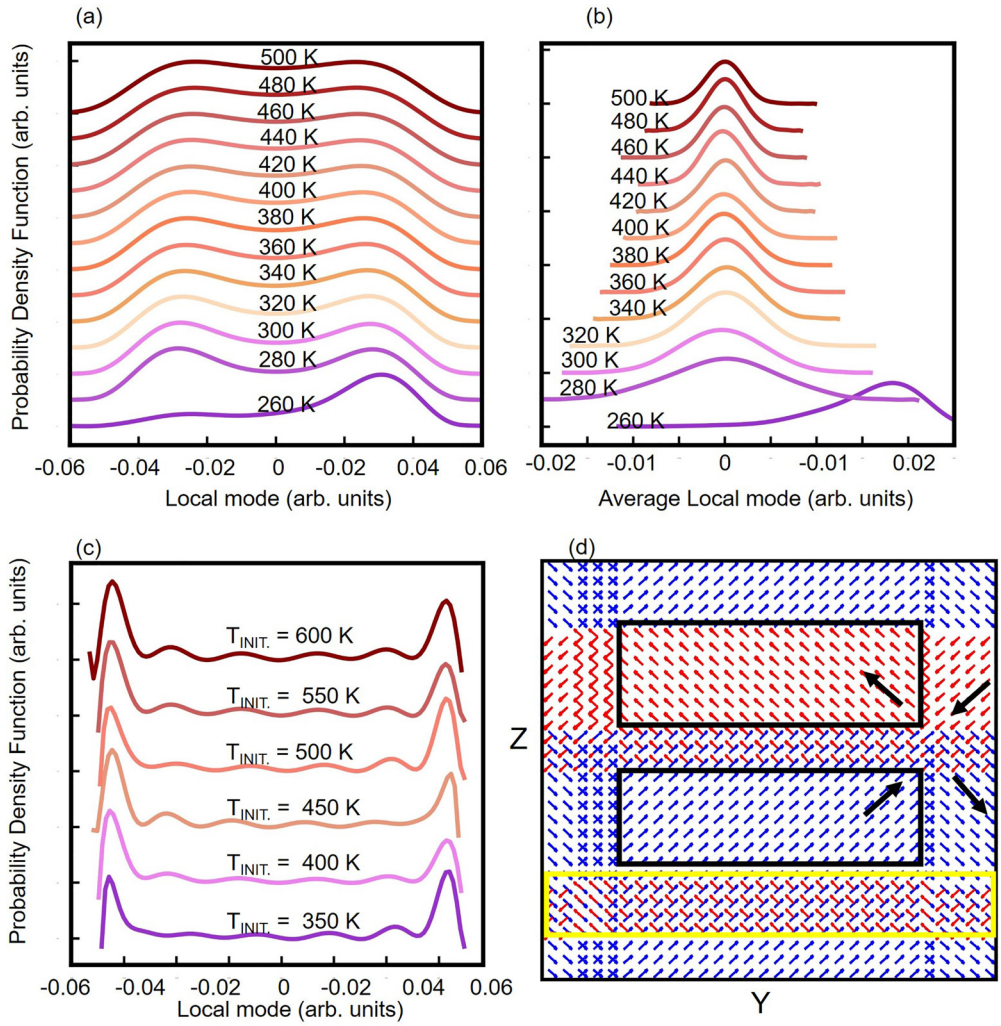

FIG. 3. (a) Probability density functions for the components of the local modes u_i and (b) for the average components $\langle u_i \rangle$ computed at different temperatures. (c) Probability density functions for the components of the local modes u_i computed for the quenched structures at 100 K. The temperature from which quenching has started is given on the labels. The dipole pattern of $CsGeBr_3$ at 100 K exhibiting polar (black boxes) and antipolar (yellow box) domains.

In summary, we developed a first-principles-based computational methodology to investigate the finite-temperature properties of ferroelectric halide perovskite $CsGeBr_3$. The application of the methodology to bulk $CsGeBr_3$ predicts a single-phase transition from the paraelectric cubic $Pm\bar{3}m$ phase to the ferroelectric rhombohedral phase $R3m$ in agreement with experimental observation. However, it also reveals a dynamical antipolar phase that exists above the Curie temperature. Such an antipolar phase can be stabilized through rapid quenching from high temperatures and can compete with the polar phase. The latter competition was found to result in the formation of polar-antipolar domains, which allow for exotic domain configurations, such as head-to-head and tail-to-tail domains, that are energetically prohibitive in traditional ferroelectrics. In fact, the only known mechanism to stabilize such head-to-head and tail-to-tail domains is through free-charge compensation. Indeed, from Poisson's equation, we have $\nabla \cdot \mathbf{P} = \rho_{\text{free}}$ in the absence of a macroscopic electric field, where ρ_{free} is the free-charge density. Since head-to-head and tail-to-tail domains are associated with polarization divergence, they can exist in the presence of a free charge, which results in charged domain walls [50]. The presence of competing antipolar phases offers a different route to such domain stabilization and may lead to new forms of topological polar structures. It is also well known that phase competition is at the origin of many enhanced responses and outstanding energy-converting properties. Some examples include a state-of-art piezoelectric coefficient in lead zirconate titanate (PZT) due to phase competition in the vicinity of the morphotropic phase boundary [51], and outstanding energy storage properties in antiferroelectrics [52]. We believe our work will promote discoveries of unusual properties and functionality associated with polar-antipolar phase competitions in halide perovskites and their applications in lead-free energy storage and conversion technology.

This work was supported by the U.S. Department of Energy, Office of Basic Energy Sciences, Division of Materials Sciences and Engineering under Grant No. DE-SC0005245.

Computational support was provided by the National Energy Research Scientific Computing Center (NERSC), a U.S. Department of Energy, Office of Science User Facility located at Lawrence Berkeley National Laboratory, operated under Contract No. DE-AC02-05CH11231 using NERSC Award No. BES-ERCAP-0025236.x

[1] R. Wang, T. Huang, J. Xue, J. Tong, K. Zhu, and Y. Yang, Nat. Photonics **15**, 411 (2021).
[2] A. Fakharuddin, M. K. Gangishetty, M. Abdi-Jalebi, S.-H. Chin, A. R. bin Mohd Yusoff, D. N. Congreve, W. Tress, F. Deschler, M. Vasilopoulou, and H. J. Bolink, Nat. Electron. **5**, 203 (2022).
[3] Z. Xiao, Y. Yuan, Y. Shao, Q. Wang, Q. Dong, C. Bi, P. Sharma, A. Gruverman, and J. Huang, Nat. Mater. **14**, 193 (2015).
[4] J. Li, J. Duan, X. Yang, Y. Duan, P. Yang, and Q. Tang, Nano Energy **80**, 105526 (2021).
[5] J. Y. Kim, J.-W. Lee, H. S. Jung, H. Shin, and N.-G. Park, Chem. Rev. **120**, 7867 (2020).
[6] E. G. Moloney, V. Yeddu, and M. I. Saidaminov, ACS Mater. Lett. **2**, 1495 (2020).
[7] B. Yang, D. Bogachuk, J. Suo, L. Wagner, H. Kim, J. Lim, A. Hinsch, G. Boschloo, M. K. Nazeeruddin, and A. Hagfeldt, Chem. Soc. Rev. **51**, 7509 (2022).
[8] A. Alaei, A. Circelli, Y. Yuan, Y. Yang, and S. S. Lee, Mater. Adv. **2**, 47 (2021).
[9] R. X. Yang, J. M. Skelton, E. L. da Silva, J. M. Frost, and A. Walsh, J. Chem. Phys. **152**, 024703 (2020).
[10] G. Thiele, H. W. Rotter, and K. D. Schmidt, Z. Anorg. Allg. Chem. **545**, 148 (1987).
[11] Y. Zhang, E. Parsonnet, A. Fernandez, S. M. Griffin, H. Huyan, C.-K. Lin, T. Lei, J. Jin, E. S. Barnard, A. Raja, P. Behera, X. Pan, R. Ramesh, and P. Yang, Sci. Adv. **8**, eabj5881 (2022).
[12] W. Zhong, D. Vanderbilt, and K. M. Rabe, Phys. Rev. Lett. **73**, 1861 (1994).
[13] W. Zhong, D. Vanderbilt, and K. M. Rabe, Phys. Rev. B **52**, 6301 (1995).
[14] U. V. Waghmare and K. M. Rabe, Phys. Rev. B **55**, 6161 (1997).
[15] L. Walizer, S. Lisenkov, and L. Bellaiche, Phys. Rev. B **73**, 144105 (2006).
[16] L. Bellaiche, A. García, and D. Vanderbilt, Phys. Rev. Lett. **84**, 5427 (2000).
[17] A. R. Akbarzadeh, S. Prosandeev, E. J. Walter, A. Al-Barakaty, and L. Bellaiche, Phys. Rev. Lett. **108**, 257601 (2012).
[18] C. Mentzer, S. Lisenkov, Z. G. Fthenakis, and I. Ponomareva, Phys. Rev. B **99**, 064111 (2019).
[19] D. Wang, J. Weerasinghe, and L. Bellaiche, Phys. Rev. Lett. **109**, 067203 (2012).
[20] B. K. Mani, S. Lisenkov, and I. Ponomareva, Phys. Rev. B **91**, 134112 (2015).
[21] H. Fu and L. Bellaiche, Phys. Rev. Lett. **91**, 257601 (2003).
[22] I. I. Naumov, L. Bellaiche, and H. Fu, Nature (London) **432**, 737 (2004).
[23] B.-K. Lai, I. Ponomareva, I. Kornev, L. Bellaiche, and G. Salamo, Appl. Phys. Lett. **91**, 152909 (2007).
[24] Q. Zhang, L. Xie, G. Liu, S. Prokhorenko, Y. Nahas, X. Pan, L. Bellaiche, A. Gruverman, and N. Valanoor, Adv. Mater. **29**, 1702375 (2017).
[25] V. Govinden, S. Rijal, Q. Zhang, Y. Nahas, L. Bellaiche, N. Valanoor, and S. Prokhorenko, Phys. Rev. Mater. **7**, L011401 (2023).
[26] B. K. Mani, C.-M. Chang, S. Lisenkov, and I. Ponomareva, Phys. Rev. Lett. **115**, 097601 (2015).
[27] C.-M. Chang, B. K. Mani, S. Lisenkov, and I. Ponomareva, Ferroelectrics **494**, 68 (2016).
[28] G. Kresse and J. Furthmüller, Comput. Mater. Sci. **6**, 15 (1996).
[29] G. Kresse and J. Furthmüller, Phys. Rev. B **54**, 11169 (1996).
[30] P. E. Blöchl, Phys. Rev. B **50**, 17953 (1994).
[31] J. P. Perdew, K. Burke, and M. Ernzerhof, Phys. Rev. Lett. **77**, 3865 (1996).
[32] A. Togo and I. Tanaka, Scr. Mater. **108**, 1 (2015).
[33] D. M. Ceperley and B. J. Alder, Phys. Rev. Lett. **45**, 566 (1980).
[34] https://github.com/USFmatscilab/CGB.
[35] See Supplemental Material at http://link.aps.org/supplemental/10.1103/PhysRevB.109.L020101 for details of the effective Hamiltonian terms, Hamiltonian parameters obtained from the r^{2}SCAN functional, and irregular domain patterns for higher cell sizes.
[36] B. K. Mani, C.-M. Chang, and I. Ponomareva, Phys. Rev. B **88**, 064306 (2013).
[37] S. Lisenkov and I. Ponomareva, Phys. Rev. B **80**, 140102(R) (2009).
[38] T. Nishimatsu, U. V. Waghmare, Y. Kawazoe, and D. Vanderbilt, Phys. Rev. B **78**, 104104 (2008).
[39] https://loto.sourceforge.net/feram/.
[40] D. C. Rapaport and D. C. R. Rapaport, *The Art of Molecular Dynamics Simulation* (Cambridge University Press, Cambridge, UK, 2004).
[41] S. Tinte, J. Íñiguez, K. M. Rabe, and D. Vanderbilt, Phys. Rev. B **67**, 064106 (2003).
[42] A. Paul, J. Sun, J. P. Perdew, and U. V. Waghmare, Phys. Rev. B **95**, 054111 (2017).
[43] Y. Zhang, J. Sun, J. P. Perdew, and X. Wu, Phys. Rev. B **96**, 035143 (2017).
[44] T. Hashimoto, T. Nishimatsu, H. Mizuseki, Y. Kawazoe, A. Sasaki, and Y. Ikeda, Jpn. J. Appl. Phys. **43**, 6785 (2004).
[45] M. Kingsland, K. A. Lynch, S. Lisenkov, X. He, and I. Ponomareva, Phys. Rev. Mater. **4**, 073802 (2020).
[46] J. W. Furness, A. D. Kaplan, J. Ning, J. P. Perdew, and J. Sun, J. Phys. Chem. Lett. **11**, 8208 (2020).
[47] V. V. Shvartsman, J. Zhai, and W. Kleemann, Ferroelectrics **379**, 77 (2009).
[48] V. V. Shvartsman and D. C. Lupascu, J. Am. Ceram. Soc. **95**, 1 (2012).
[49] Y. Cheng, Z. Gao, K. H. Ye, H. W. Park, Y. Zheng, Y. Zheng, J. Gao, M. H. Park, J.-H. Choi, K.-H. Xue, C. S. Hwang, and H. Lyu, Nat. Commun. **13**, 645 (2022).
[50] P. S. Bednyakov, B. I. Sturman, T. Sluka, A. K. Tagantsev, and P. V. Yudin, npj Comput. Mater. **4**, 65 (2018).
[51] N. Zhang, H. Yokota, A. M. Glazer, Z. Ren, D. A. Keen, D. S. Keeble, P. A. Thomas, and Z.-G. Ye, Nat. Commun. **5**, 5231 (2014).
[52] Z. Liu, T. Lu, J. Ye, G. Wang, X. Dong, R. Withers, and Y. Liu, Adv. Mater. Technol. **3**, 1800111 (2018).